



Various Features of the X-class White-light Flares in Super Active Region NOAA 13664

Ying Li^{1,2}, Xiaofeng Liu^{1,2}, Zhichen Jing^{1,2}, Wei Chen^{1,2}, Qiao Li^{1,2}, Yang Su^{1,2}, De-Chao Song¹,
M. D. Ding^{3,4}, Li Feng^{1,2}, Hui Li^{1,2}, and Weiqun Gan^{1,5}

¹ Key Laboratory of Dark Matter and Space Astronomy, Purple Mountain Observatory, CAS, Nanjing 210023, People's Republic of China; yingli@pmo.ac.cn

² School of Astronomy and Space Science, University of Science and Technology of China, Hefei 230026, People's Republic of China

³ School of Astronomy and Space Science, Nanjing University, Nanjing 210023, People's Republic of China

⁴ Key Laboratory for Modern Astronomy and Astrophysics (Nanjing University), Ministry of Education, Nanjing 210023, People's Republic of China

⁵ University of Chinese Academy of Sciences, Nanjing 211135, People's Republic of China

Received 2024 June 13; revised 2024 July 31; accepted 2024 August 9; published 2024 August 21

Abstract

Super active region NOAA 13664 produced 12 X-class flares (including the largest one so far, an occulted X8.7 flare, in solar cycle 25) during 2024 May 8–15, and 11 of them are identified as white-light flares. Here we present various features of these X-class white-light flares observed by the White-light Solar Telescope (WST) on board the Advanced Space-based Solar Observatory and the Helioseismic and Magnetic Imager (HMI) on board the Solar Dynamics Observatory. It is found that both the white-light emissions at WST 3600 Å (Balmer continuum) and HMI 6173 Å (Paschen continuum) show up in different regions of the sunspot group in these flares, including outside the sunspots and within the penumbra and umbra of the sunspots. They exhibit a point-, ribbon-, loop-, or ejecta-like shape, which can come from flare ribbons (or footpoints), flare loops, and plasma ejecta depending on the perspective view. The white-light duration and relative enhancement are measured and both parameters for 3600 Å emission have greater values than those for 6173 Å emission. It is also found that these white-light emissions are cospatial well with the hard X-ray (HXR) sources in the on-disk flares but have some offsets with the HXR emissions in the off-limb flares. In addition, it is interesting that the 3600 and 6173 Å emissions show different correlations with the peak HXR fluxes, with the former one more sensitive to the HXR emission. All these greatly help us understand the white-light flares of a large magnitude from a super active region on the Sun and also provide important insights into superflares on Sun-like stars.

Unified Astronomy Thesaurus concepts: [Solar activity \(1475\)](#); [Solar white-light flares \(1983\)](#); [Solar active regions \(1974\)](#); [Solar chromosphere \(1479\)](#); [Solar x-ray emission \(1536\)](#)

1. Introduction

Solar white-light flares (WLFs) are a special kind of flare, which show an enhancement in the visible continuum. The first reported solar flare, i.e., the Carrington event in 1859 (Carrington 1859; Hodgson 1859), was a well-known WLF. After that, several hundreds of solar WLFs were observed in spatially resolved images and also multiwavelength spectra with ground- and space-based telescopes. It has been found that solar WLFs are similar to stellar flares in many aspects (e.g., Worden 1983), the latter of which are mainly observed in light curves by Kepler and Transiting Exoplanet Survey Satellite in the optical wave band (e.g., Pugh et al. 2016). Therefore, studying solar WLFs via images in detail can provide invaluable insights into stellar flares.

Solar WLFs are generally categorized into two types based on their observational features (e.g., Fang & Ding 1995; Ding 2007). Type I WLFs display enhanced Balmer continua (or a Balmer jump) and prominent Balmer lines, which are usually associated well with the hard X-ray (HXR) emissions. Type II WLFs rarely show those features, though some of them may also be accompanied by HXR emissions (Procházka et al. 2018). The white-light (WL) emissions can be caused by a nonthermal electron-beam heating (e.g., Hudson 1972; Krucker et al. 2015) and its secondary effect, such as radiative

backwarming (Gan & Mauas 1994; Ding et al. 2003; Xu et al. 2004) and chromospheric condensation (Gan et al. 1992; Kowalski et al. 2015). Some other mechanisms such as a proton-beam heating (Machado et al. 1978; Hiei 1982; Procházka et al. 2018), X-ray and EUV irradiations (Henoux & Nakagawa 1977; Poland et al. 1988), and Alfvén waves (Emslie & Sturrock 1982; Fletcher & Hudson 2008) can also contribute to the WL emissions in solar flares.

Super active regions (ARs) have been studied for a few solar cycles (e.g., Chen et al. 2011; Le et al. 2014), which can produce numerous flares including some largest ones in that solar cycle. The top largest flares (say, above X5.0) in a super AR are supposed to be WLFs (Neidig & Cliver 1983), for example, the X9.3 flare on 2017 September 6 from NOAA 12673 in solar cycle 24 (Romano et al. 2018). It should be noted that the AR that produced the Carrington WLF is a super one whose sunspot area was greater than 2400 millionths of the solar hemisphere (MSH; the whole sunspot group being 2971 MSH. Hayakawa et al. 2023). In the current solar cycle 25, there has appeared a super AR numbered as NOAA 13664, whose maximum area reached 2761 MSH (Hayakawa et al. 2024), i.e., comparable with the Carrington AR. NOAA 13664 produced 12 X-class and ~62 M-class flares when it crossed the visible solar disk from 2024 May 1 to May 15. This region along with its 12 X-class flares were well observed by the Advanced Space-based Solar Observatory (ASO-S; Gan et al. 2023) and the Solar Dynamics Observatory (SDO; Pesnell et al. 2012). In particular, 11 of the X-class flares (excluding the first X1.0) are identified as WLFs.

Table 1
Information of the 12 X-class Flares from Super AR NOAA 13664

Flare No.	Observation Date (yyyy-mm-dd)	GOES Start (UT)	GOES Peak (UT)	GOES End (UT)	GOES Class	AR Location	Remarks
FL1	2024-05-08	04:37	05:09	05:28	X1.0	S22W11	on-disk, NWLF
FL2	2024-05-08	21:08	21:40	21:58	X1.0	S20W17	on-disk, “WLF” ^a
FL3	2024-05-09	08:45	09:13	09:31	X2.3	S20W24	on-disk, WLF
FL4	2024-05-09	17:23	17:44	18:01	X1.1	S17W28	on-disk, WLF
FL5	2024-05-10	06:27	06:54	07:13	X4.0	S17W34	on-disk, WLF
FL6	2024-05-11	01:10	01:23	01:39	X5.8	S17W44	on-disk, WLF
FL7	2024-05-11	11:15	11:44	12:01	X1.5	S19W60	on-disk, WLF
FL8	2024-05-12	16:11	16:26	16:43	X1.0	S20W75	on-disk, WLF
FL9	2024-05-14	02:03	02:09	02:19	X1.7	S17W89	on-limb, WLF
FL10	2024-05-14	12:40	12:55	13:05	X1.2	S17W89	off-limb, WLF
FL11	2024-05-14	16:46	16:51	17:02	X8.7	S18W89	off-limb, WLF
FL12	2024-05-15	08:18	08:37	08:55	X3.5	S18W89	off-limb, WLF

Note.

^a “WLF” means that this flare has some detectable brightening at 3600 Å but its relative enhancement is below our threshold of 8%.

In this Letter, we focus on the 12 X-class flares, especially on the 11 WLFs among them, which occurred in the super AR NOAA 13664 during 2024 May 8–15. Thanks to the routine full-disk imaging observations from the White-light Solar Telescope (WST) on the Ly α Solar Telescope (LST; Feng et al. 2019; Li et al. 2019; Chen et al. 2024) on board ASO-S and the Helioseismic and Magnetic Imager (HMI; Scherrer et al. 2012) on board SDO, we can study the emission features of these X-class WLFs at 3600 and 6173 Å (i.e., below and above the Balmer limit) simultaneously. Properties of the WL emissions including their morphology, source, duration, and enhancement are presented in this study, together with their physical origins. All these can significantly improve our understanding of the solar WLFs and further provide important insights into superflares on the Sun-like stars.

2. Observational Data

The WL continuum data used in this work are obtained by SDO/HMI and ASO-S/WST. WST provides the full-disk imaging data at 3600 Å (in the Balmer continuum) with a cadence of 2 minutes routinely. The images have a pixel size of $\sim 0''.5$, whereas the spatial resolution is $\sim 4''$ due to a poor point-spread function. HMI obtains the magnetogram data via the Fe I line at 6173 Å as well as pseudo-continuum (Paschen continuum) images near the line, which have a pixel size of $0''.5$ and a cadence of 45 s. We also use the HXR data observed by the Hard X-ray Imager (HXI; Zhang et al. 2019; Su et al. 2022) on ASO-S and some EUV/UV images from the Atmospheric Imaging Assembly (AIA; Lemen et al. 2012) on SDO. HXI observes the full Sun in an energy range of ~ 10 –300 keV. Its energy and angular resolutions are $\sim 16.5\%$ at 32 keV and $3''.1$, respectively. AIA provides the EUV/UV images at 131, 94, 335, 193, 211, 171, 304, 1600, and 1700 Å with a cadence of 12 or 24 s. These images have a pixel size of $0''.6$ and the spatial resolution is $1''.2$. The soft X-ray (SXR) flux at 1–8 Å observed by the X-Ray Sensor (XRS; Hanser & Sellers 1996) on the Geostationary Operational Environmental Satellite (GOES) is presented in this work as well, which is used to divide the flares into A, B, C, M, and X classes.

3. Observations and Results

3.1. Overview of the 12 X-class Flare Events in Super AR NOAA 13664

The 12 X-class flares, labeled as FL1 to FL12 (see Table 1), occurred in the super AR NOAA 13664 during 2024 May 8–15. NOAA 13664 appeared at the solar east limb on May 1, reached a sunspot area of ~ 2400 MSH on May 11 with a $\beta\gamma\delta$ /Fkc sunspot group, and rotated over the west limb on May 15. This region produced numerous flares (including the largest X8.7 in the solar cycle 25 so far) as seen from the GOES SXR 1–8 Å light curve in Figure 1(a). Figure 1(b) shows the AIA 1600 and 131 Å images around the peak times of these X-class flares. One can see that most of the events (i.e., on-disk FL1–FL8) show clear ribbons and hot flaring loops. When the region rotated over the west limb, only flare loops were visible above the limb (in the off-limb FL10–FL12).

Among the 12 X-class flares, 11 are identified as WLFs (see the remarks in Table 1), and only the first X1.0 flare (FL1) is not a detectable WLF (NWLF). Here we define a WLF using intensity thresholds (a ratio of the intensity at a single flaring pixel and the average intensity over a quiet-Sun region near the flaring region) of 5% for HMI 6173 Å emissions (Song et al. 2018) and 8% for WST 3600 Å emissions (Jing et al. 2024) for the on-disk flares, i.e., FL1–FL8. These threshold values are about 3 times the intensity fluctuations or standard deviations of the intensity over the nearby quiet-Sun region during the whole flare time, which are within 1.4% and 2.9% for HMI and WST, respectively. Note that the second X1.0 flare (FL2) shows some reliable brightening at WST 3600 Å (marked by the red arrow in Figure 3(b)) but its intensity ratio is actually below the above thresholds. For the on- and off-limb events of FL9–FL12, since their WL brightenings are relatively weak, we just identify them as WLFs by checking the base-difference images (see Figure 3) by eye. From Figure 2 it is seen that the 3600 Å brightening can be visible in the original WST images for some large or on-limb flares, say, FL5 (X4.0), FL6 (X5.8), and FL9 (X1.7), while in the other WLFs the 3600 and 6173 Å brightenings can only be seen from the base- or running-difference images as shown in Figure 3.

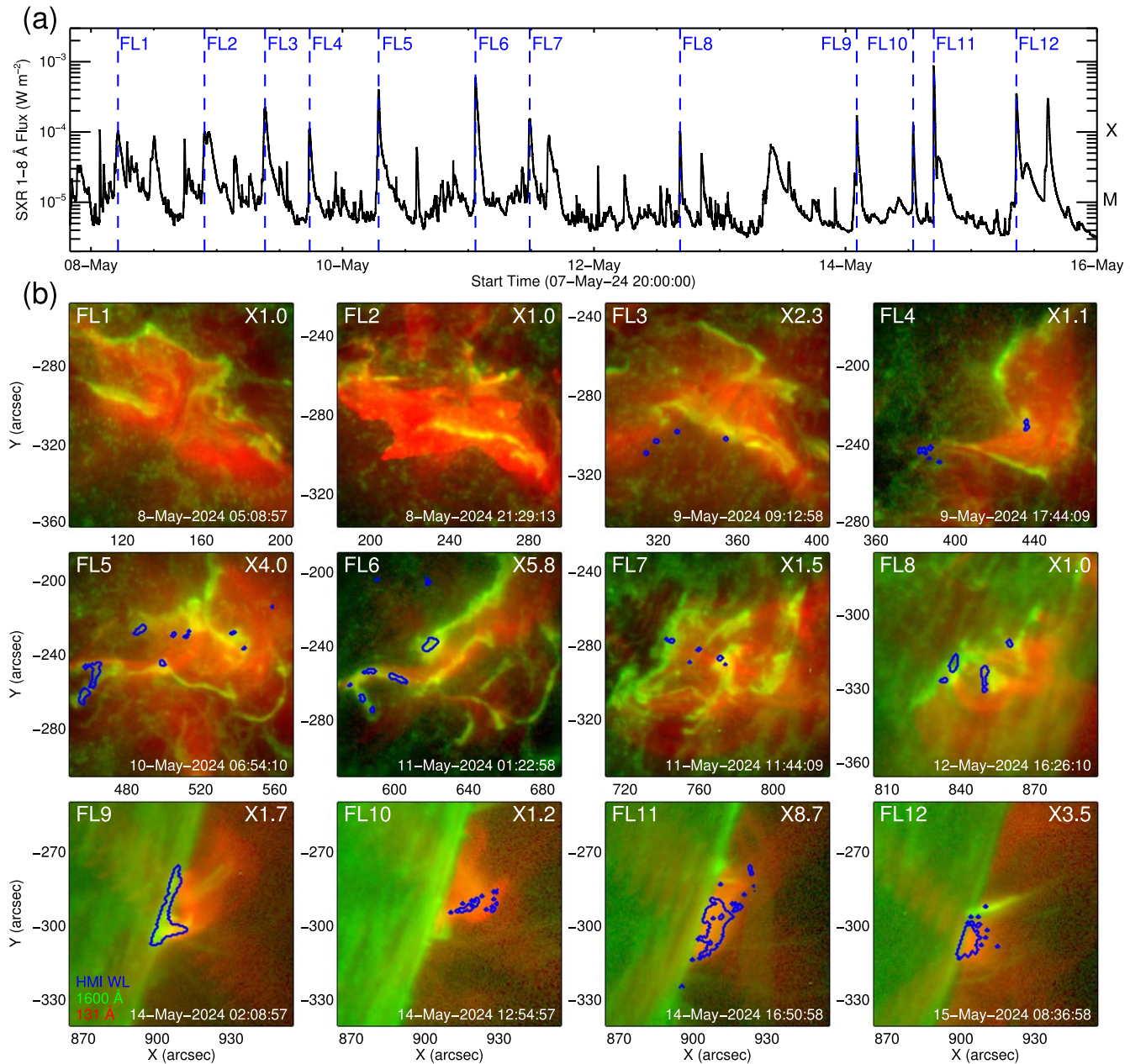


Figure 1. Overview of the 12 X-class flare events in super AR NOAA 13664. (a) GOES SXR flux during 2024 May 7–16. The blue vertical dashed lines in the panel denote the peak times of the 12 X-class flares. (b) AIA 1600 Å (green) and 131 Å (red) images around the peak times of the 12 flares. The blue contours in the images mark the HMI 6173 Å brightenings, which are the same as the red contours in Figure 2(a).

3.2. Properties of the WL Emissions at WST 3600 Å and HMI 6173 Å

3.2.1. WL Morphology and Source

From Figure 2 (the red contours marking the WL brightenings) one can see that the bright 6173 and 3600 Å emissions show up in different regions of the sunspot group. In some WLFs, these two wave band brightenings mainly appear outside the sunspots, say, in FL2 and FL3. By contrast, the brightenings can be located in the penumbra or even umbra of the sunspots in FL4–FL9. In the off-limb WLFs of FL10–FL12 with their footpoints occulted by the solar limb, the WL emissions are mainly seen above the limb or in the corona.

From Figure 3 (and also the red contours in Figure 2) we can see that the bright emissions at 6173 and especially 3600 Å display various shapes in the morphology (also listed in Table 2). In FL2–FL4, FL7, and FL8 (all $< X3.0$), the WL brightenings mainly show a pointlike shape, say, a single point (FL2), double points (FL4), and even three points (FL7 and FL8). By contrast, the bright emissions in FL5 and FL6 ($\geq X4.0$) show a ribbon-like shape. Note that the brightening area and also the enhancement at 6173 Å are smaller than those at 3600 Å (see the following section). These on-disk WL emissions in FL2–FL8 are mainly located at the flare footpoints or ribbons combined with the AIA 1600 Å images in Figure 1(b). Note that the times of the WL and 1600 Å emissions are not exactly the same. In the remaining four on- or

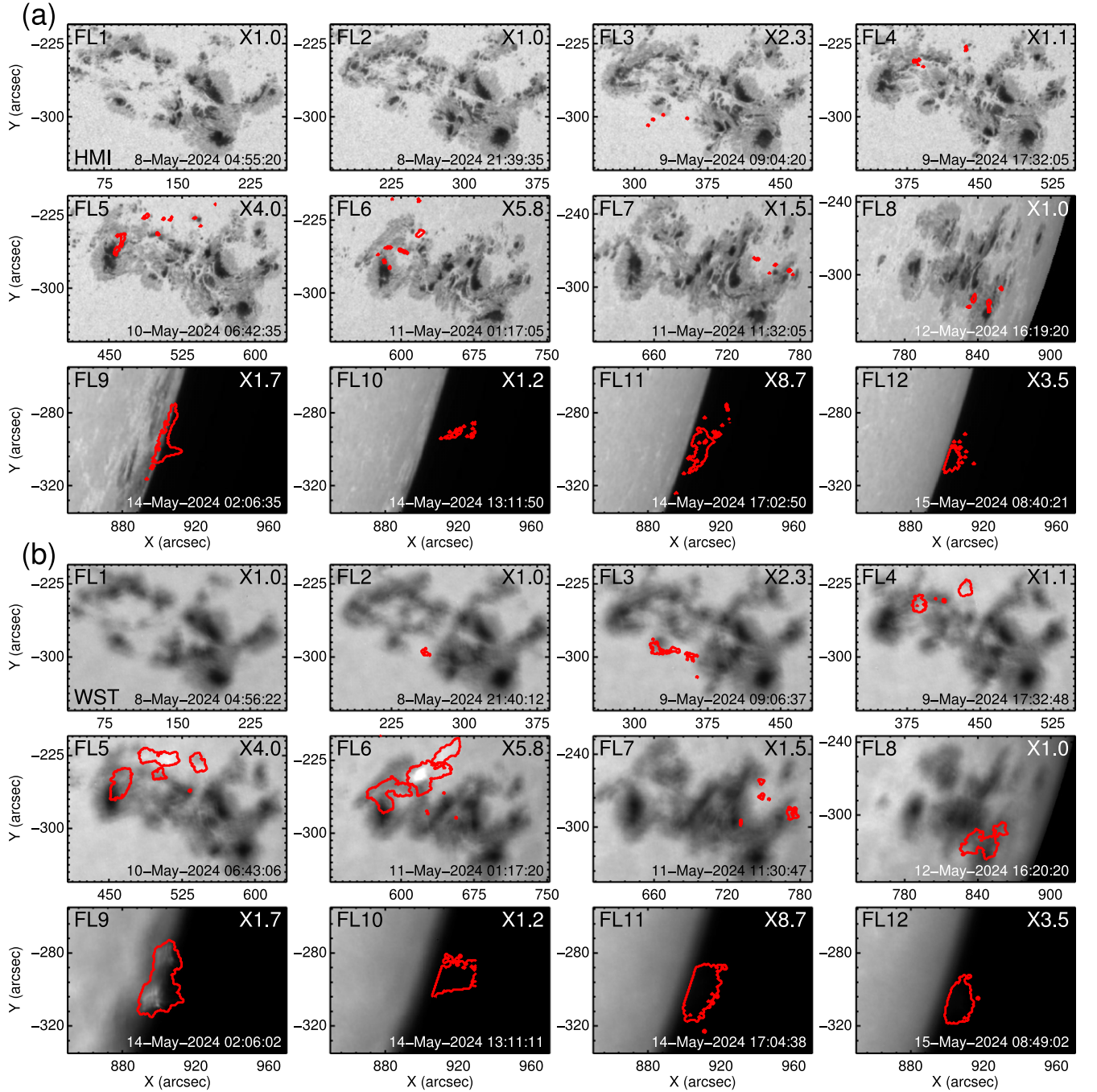


Figure 2. HMI (a) and WST (b) images at the WL brightening time for the 12 X-class flares. The red contours with fixed levels for on-disk (except FL3 and FL7 having a weak WL emission) and off-limb flares, respectively, in the images indicate the WL brightenings that correspond to those as seen in the running- or base-difference images in Figure 3. Note that FL1 is not a detectable WLF without showing the WL contours and that FL2 without the HMI contour is due to data missing during its WL brightening period.

off-limb flares (FL9–FL12), the WL emissions exhibit a loop- or ejecta-like shape, corresponding to the flare loop structures in the corona as seen in AIA 131 Å images in Figure 1(b). Note that in the on-limb FL9, the WL brightening is also from chromospheric footpoints.

3.2.2. WL Enhancement and Duration

The relative enhancement of WL emission is defined as $(I - I_{\text{ref}})/I_{\text{ref}}$, where I and I_{ref} are the WL intensity during the flare and the reference intensity, respectively. For WST, we adopt the average intensity over 10 minutes during the preflare

phase as I_{ref} , while the average intensity over the 15–9 minutes before the WL peak time is used as I_{ref} for HMI in order to avoid the sunspot motion effect as much as possible. We provide the enhancements of both HMI 6173 Å and WST 3600 Å emissions averaged over the maximum WL area for the on-disk WLFs, as listed in Table 2. Here the uncertainties or errors are derived by varying the intensity thresholds of identifying a WLF, say, $5 \pm 1.02\%$ and $8 \pm 1.26\%$, where 1.02% and 1.26% are the averaged standard deviations of the intensity fluctuations over a quiet-Sun region for HMI and WST, respectively. It is seen that the enhancement of 3600 Å

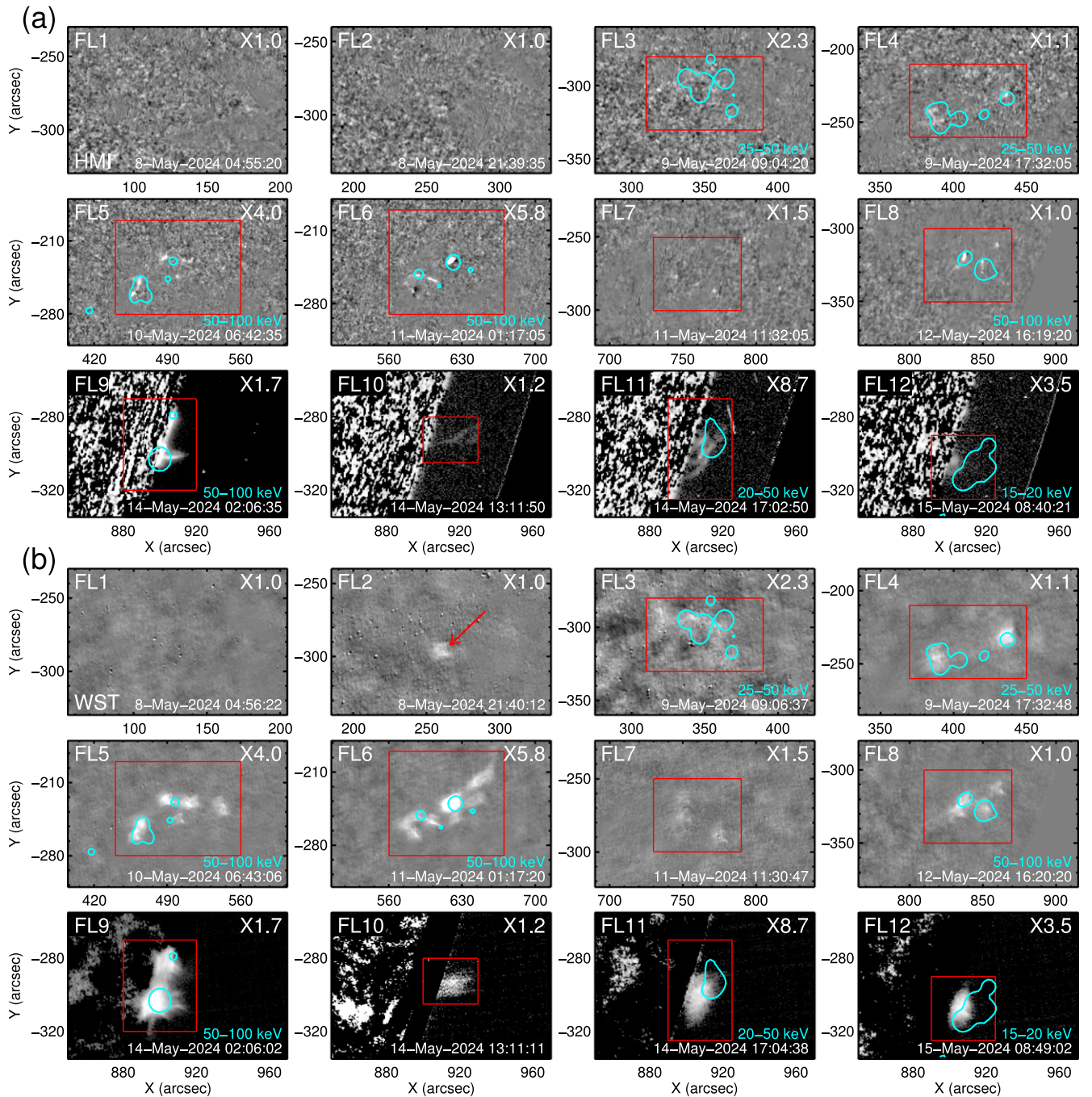


Figure 3. HMI (a) and WST (b) running- (for on-disk flares) or base-difference (for off-limb flares) images at the WL brightening time for the 12 X-class flares. The cyan contours (with 20% level at the maximum) in the images mark the HXI HXR sources for the WLFs that have available HXI data at the corresponding time. The red boxes denote the regions integrated over for the HMI and WST emission curves in Figure 4. The red arrow in the WST image of FL2 indicates the visible 3600 Å brightening though its enhancement is below our threshold.

emission is greater than that of 6173 Å in all FL3–FL8, i.e., type I WLFs basically. The former has a range of 13%–27%, while the latter is 9%–15%. These enhancements are similar to those reported in Song et al. (2018) and Jing et al. (2024) though most of the WLFs in both studies are M-class ones. For the on- and off-limb WLFs, they could be referred to as coronal type (listed in Table 2) due to the WL emissions appearing in the corona.

The WL duration is measured from the WST plus HMI light curve. Figure 4 plots the normalized WL curves at 6173 and 3600 Å integrated over the flaring region marked by the red

box in Figure 3 for FL3–FL12. Note that FL7 exhibits a very weak brightening at 6173 Å, which is not obvious in the integrated light curve, thus the HMI curve is not shown here. It is seen that the two wave band emission curves display a very similar trend in the majority of the WLFs. Based on these WL curves, together with the WST images in which the brightening is easier to be seen, we determine the WL duration just by eye. The results are shown with a yellow shaded area in Figure 4 and also listed in Table 2. One can see that except FL2, all the identified WLFs have a duration of longer than 15 minutes with a range of ~16–44 minutes. Note that the durations determined

Table 2
Properties of the WL Emissions for the 11 WLFs along with Their Peak HXR Fluxes

Flare No.	GOES Class	WL Morphology	WL Source	WL Duration (min)	WL Enhancement ^a (%)		WL Ratio (3600/6173)	Type	$F_{p,20-50}$ ^c (counts s ⁻¹ keV ⁻¹ cm ⁻²)	$F_{p,50-100}$ ^d
					HMI 6173 Å	WST 3600 Å				
FL2	X1.0	pointlike	footpoints	≤2	... ^b	<8	1.77	~0.35
FL3	X2.3	pointlike	footpoints	~44	10.9 ± 2.17	16.9 ± 2.59	1.56 ± 0.57	type I	5.63	~0.61
FL4	X1.1	pointlike	footpoints	~16	9.46 ± 1.97	14.1 ± 1.68	1.49 ± 0.51	type I	10.8	~0.47
FL5	X4.0	ribbon-like	footpoints	~28	11.3 ± 2.32	18.9 ± 1.61	1.68 ± 0.51	type I	33.0	1.75
FL6	X5.8	ribbon-like	footpoints	~22	10.9 ± 1.86	22.7 ± 3.49	2.08 ± 0.69	type I	74.0	1.37
FL7	X1.5	pointlike	footpoints	~21	9.27 ± 1.43	13.5 ± 2.59	1.45 ± 0.52	type I	~10.0	~0.44
FL8	X1.0	pointlike	footpoints	~20	15.0 ± 4.19	26.5 ± 3.14	1.77 ± 0.77	type I	38.8	2.49
FL9	X1.7	point- and loop-like	footpoints and loops	~18	coronal
FL10	X1.2	loop-like	loops	~20	coronal
FL11	X8.7	loop-like	loops	~24	coronal
FL12	X3.5	loop-like	loops	~36	coronal

Notes.

^a The WL enhancement refers to the one averaged over the maximum WL area.

^b The HMI data during the WL brightening period (~21:39–21:44 UT) were missing.

^c $F_{p,20-50}$ represents the peak HXR flux at 20–50 keV.

^d $F_{p,50-100}$ represents the peak HXR flux at 50–100 keV.

by eye here are likely to be overestimated for the HMI 6173 Å emission, which usually exhibits a weaker enhancement and has a smaller brightening area. Our results are indeed greater than the durations (only about 5 minutes) reported in Song et al. (2018) for 6173 Å emissions. It should also be mentioned that our durations are fairly similar to those measured by Jing et al. (2024) for 3600 Å emissions in M-class and especially X-class WLFs.

3.2.3. Relationship of the WL brightening with the HXR Emission

First, we check the spatial relationship between the WL and HXR emissions. The HXR images are obtained via the HXI CLEAN algorithm (Su et al. 2019) and their contours are overplotted on the running- or base-difference images of HMI and WST in Figure 3. Note that the HXR images of FL7 and FL10 are not provided mainly due to the corresponding HXR data being unavailable at that time. From Figure 3 one can see that in the on-disk/limb WLFs (FL3–FL6, FL8, and FL9), the WL brightenings are cospatial with the HXR footpoint sources well. For the two off-limb WLFs (FL11 and FL12), the WL emissions are mostly under the HXR looptop sources with some offsets. These will be discussed in the following section.

Then, we check the temporal relationship between the WL and HXR emissions, which shows various cases. Figure 4 plots the background-subtracted HXR light curves at 10–20, 20–50, 50–100, and 100–200 keV from HXI. One could see that in FL3, the 6173 and 3600 Å emissions seem to peak later than the HXR emissions at 10–20 and 20–50 keV and even later than the SXR 1–8 Å emission. Here it should be noted that the HMI and WST emission curves for this flare show an oscillation pattern and the images look somewhat noiselike (Figure 3). Moreover, the current cadences of HMI and WST might not be high enough to determine the true peaks. For FL4, the HMI and WST emissions seem to reach the maximum around the same time as the HXR emission at 20–50 keV and before the SXR emission. Note that here we overplot the HMI emission curve integrated over the WL sources only for reference (see the gray curve). In FL5, FL6, FL8, and FL9, the

WL emissions peak around the same time as the HXR 50–100 keV emission (and also HXR 100–200 keV) in the rise phase of the flare. For the off-limb FL10–FL12, their WL emissions reach the maximum during the decay phase and much later than the HXR emissions mainly due to the footpoints being occulted.

Finally, it is interesting to find that the WL enhancements have some good correlations with the peak SXR as well as HXR fluxes (listed in Table 2) and particularly that the 6173 and 3600 Å emissions show different dependencies on the HXR emissions. In FL3–FL8, their 3600 Å enhancements have good correlations with their peak HXR fluxes at 20–50 and 50–100 keV, with correlation coefficients (cc) of 0.73 and 0.91, respectively. While the 6173 Å enhancements only show a good correlation (cc = 0.91) with the peak HXR flux at 50–100 keV. Moreover, the enhancement ratios of 3600 and 6173 Å emissions have some relationships with the peak HXR fluxes at 20–50 keV (cc = 0.98) and 50–100 keV (cc = 0.59) and also peak SXR flux (cc = 0.76) in these WLFs.

4. Summary and Discussions

In this study, we present various features of 11 X-class WLFs observed by ASO-S and SDO during 2024 May 8–15, which occurred in the super AR NOAA 13664 in the current solar cycle 25. Thanks to the routine full-disk imaging observations of ASO-S/WST at 3600 Å and SDO/HMI at 6173 Å, we can investigate the Balmer and Paschen continuum emissions simultaneously and compare them with each other in these large magnitude WLFs. Our results are summarized as follows.

1. In total, 11 out of the 12 X-class flares (except the first X1.0) are identified as WLFs. Their bright 6173 and 3600 Å emissions show up in different regions of the sunspot group, including outside the sunspots and within the penumbra and umbra of the sunspots.
2. The 6173 and 3600 Å brightenings exhibit various shapes such as point-, ribbon-, loop-, and ejecta-like and can

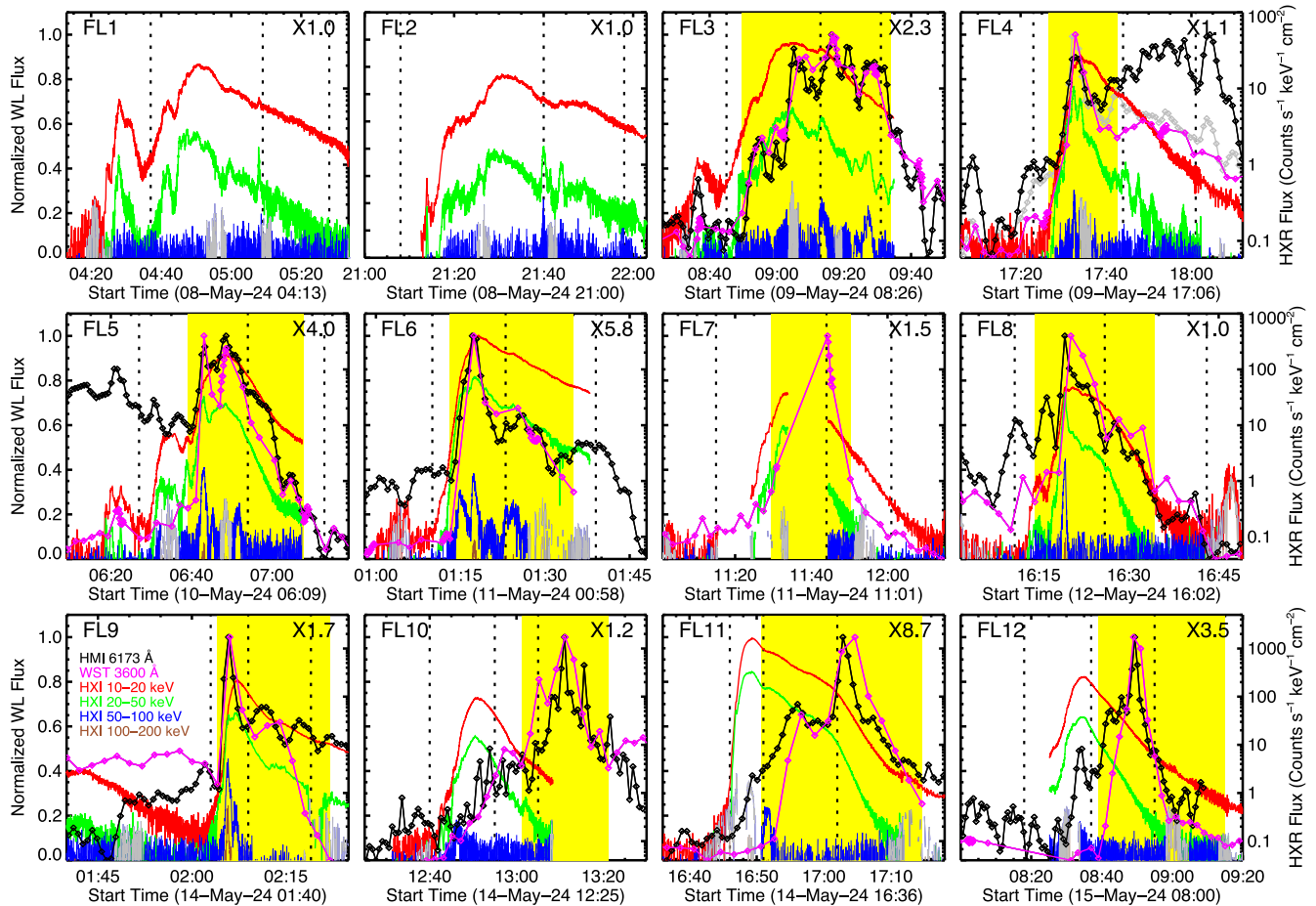


Figure 4. HXR and WL emission curves from HXI, HMI, and WST for the 12 X-class flares. The HMI and WST emissions are integrated over the same flaring region marked by the red box in Figure 3. For FL4, we also overplot the HMI emission curve (in gray) integrated over the compact WL sources only for reference. In each panel, the three vertical dotted lines indicate the flare onset, peak, and end times. The yellow shaded area denotes the duration of the WL emission at WST 3600 Å. Note that the time periods affected by the radiation belt are indicated in gray in the HXR 50–100 keV curve and that the poor HXR data during the times of the South Atlantic Anomaly (SAA) and HXI night are not displayed.

come from flare footpoints/ribbons mainly rooted in the chromosphere (some might be deep into the photosphere) and also from flare loops in the corona.

3. The relative enhancement of 3600 Å emissions is greater than that of 6173 Å emissions for the on-disk WLFs, with the former in a range of 13%–27% and the latter of 9%–15%. The duration of 3600 Å emissions ranges from 16 to 44 minutes, which is supposed to be longer than that of 6173 Å emissions.
4. The 3600 and 6173 Å brightenings are cospatial well with the HXR sources in the on-disk WLFs, which, however, have some offsets with the HXR emissions in the off-limb WLFs. These WL emissions can peak around the same time or (much) later than the HXR emission. It is also interesting that the 3600 and 6173 Å emissions show different dependencies on the peak HXR fluxes, with the former one more sensitive to the HXR emission.

According to the spatial relationship between the WL and HXR emissions, we speculate that the 3600 and also 6173 Å emissions at flare footpoints are closely related to an electron-beam heating (e.g., Song et al. 2023) that mainly happens in the rise phase of the flare. This can explain a good match of the peak times of WL and HXR emissions in some of the WLFs. The secondary effect of the beam heating, such as radiative

backwarming, can also contribute to the 3600 and especially 6173 Å emissions (e.g., Hao et al. 2017), which usually causes a delay between the WL and HXR emissions in some of the other WLFs. As regards the 3600 and 6173 Å emissions on flare loops during the decay phase, which show a spatial offset with the HXR sources, they are supposed to be related to thermal plasma cooling (e.g., Li et al. 2024) or due to Thomson scattering (e.g., Hiei et al. 1992; Saint-Hilaire et al. 2014; Heinzel et al. 2017). Note that here we could not exclude that cool plasma ejecta generates the WL emissions above the limb (e.g., Martínez Oliveros et al. 2014; Saint-Hilaire et al. 2014; Fremstad et al. 2023). Overall, the relationships between the WL and HXR emissions show various cases, thus revealing various mechanisms responsible for the WL emissions in these X-class WLFs.

The 11 X-class WLFs together with the first non-WLF (or NWLF) exhibit some interesting developing trends as the super AR evolves over time. (1) The first X1.0 flare is not a detectable WLF, while the second X1.0 flare begins to show a short and visible 3600 Å brightening (still below our threshold). Then all the following X-class flares exhibit 3600 and 6173 Å emissions above the thresholds. (2) The WL emissions at 6173 and 3600 Å appear outside the sunspots (or in a quiet-Sun region) in the first few WLFs, which begin to show up












within the penumbra and even umbra in the following WLFs. (3) The HXR emissions can only be visible mainly at 20–50 keV in the first few flares, which become notable at 50–100 keV and even 100–200 keV in the following on-disk or on-limb flares. (4) As the AR rotated over the west limb, the WL emissions can be seen from the chromospheric footpoints to flare loops in the corona. The former three should be related to the time evolution of the magnetic and sunspot complexity of this super AR, which is worthwhile to study in the future.

The routine full-disk imaging observations of WST and HMI give us good opportunities to systematically investigate the Balmer and Paschen continuum emissions at 3600 and 6173 Å, respectively, in WLFs. In particular, the 3600 and 6173 Å emissions show various features in the 11 X-class WLFs from this single super AR. These provide important constraints for the radiative hydrodynamic modeling of solar and stellar flares, especially combined with spectroscopic observations from the Chinese H α Solar Explorer (Li et al. 2022) and the Interface Region Imaging Spectrograph (De Pontieu et al. 2014), which will help us well understand the energy transportation and deposition of WLFs (Heinzel & Kleint 2014; Kleint et al. 2016).

Acknowledgments

We appreciate the referee's valuable suggestions and comments that helped to improve our manuscript. The ASO-S mission is supported by the Strategic Priority Research Program on Space Science, Chinese Academy of Sciences. SDO is a mission of NASA's Living With a Star Program. The authors are supported by the Strategic Priority Research Program of the Chinese Academy of Sciences under grant XDB0560000, the National Key R&D Program of China under grant 2022YFF0503004, and NSFC under grants 12273115, 12233012, and 11921003.

ORCID iDs

Ying Li  <https://orcid.org/0000-0002-8258-4892>
 Xiaofeng Liu  <https://orcid.org/0000-0002-3657-3172>
 Zhichen Jing  <https://orcid.org/0000-0002-8401-9301>
 Wei Chen  <https://orcid.org/0000-0001-5279-3266>
 Qiao Li  <https://orcid.org/0000-0001-7540-9335>
 Yang Su  <https://orcid.org/0000-0002-4241-9921>
 De-Chao Song  <https://orcid.org/0000-0003-0057-6766>
 M. D. Ding  <https://orcid.org/0000-0002-4978-4972>
 Li Feng  <https://orcid.org/0000-0003-4655-6939>
 Hui Li  <https://orcid.org/0000-0003-1078-3021>
 Weiqun Gan  <https://orcid.org/0000-0001-9979-4178>

References

- Carrington, R. C. 1859, *MNRAS*, **20**, 13
 Chen, B., Feng, L., Zhang, G., et al. 2024, arXiv:2408.01937
 Chen, A. Q., Wang, J. X., Li, J. W., et al. 2011, *A&A*, **534**, A47
 De Pontieu, B., Title, A. M., Lemen, J. R., et al. 2014, *SoPh*, **289**, 2733
 Ding, M. D. 2007, in ASP Conf. Ser. 368, *The Physics of Chromospheric Plasmas*, ed. P. Heinzel, I. Dorotovič, & R. J. Rutten, 368 (San Francisco, CA: ASP), 417
 Ding, M. D., Liu, Y., Yeh, C.-T., et al. 2003, *A&A*, **403**, 1151
 Emslie, A. G., & Sturrock, P. A. 1982, *SoPh*, **80**, 99
 Fang, C., & Ding, M. D. 1995, *A&AS*, **110**, 99
 Feng, L., Li, H., Chen, B., et al. 2019, *RAA*, **19**, 162
 Fletcher, L., & Hudson, H. S. 2008, *ApJ*, **675**, 1645
 Fremstad, D., Guevara Gómez, J. C., Hudson, H., et al. 2023, *A&A*, **672**, A32
 Gan, W., Zhu, C., Deng, Y., et al. 2023, *SoPh*, **298**, 68
 Gan, W. Q., & Mauas, P. J. D. 1994, *ApJ*, **430**, 891
 Gan, W. Q., Rieger, E., Zhang, H. Q., et al. 1992, *ApJ*, **397**, 694
 Hanser, F. A., & Sellers, F. B. 1996, *Proc. SPIE*, **2812**, 344
 Hao, Q., Yang, K., Cheng, X., et al. 2017, *NatCo*, **8**, 2202
 Hayakawa, H., Bechet, S., Clette, F., et al. 2023, *ApJL*, **954**, L3
 Hayakawa, H., Ebihara, Y., Mishev, A., et al. 2024, arXiv:2407.07665
 Heinzel, P., & Kleint, L. 2014, *ApJL*, **794**, L23
 Heinzel, P., Kleint, L., Kašparová, J., et al. 2017, *ApJ*, **847**, 48
 Henoux, C., & Nakagawa, Y. 1977, *A&A*, **57**, 105
 Hiei, E. 1982, *SoPh*, **80**, 113
 Hiei, E., Nakagomi, Y., & Takuma, H. 1992, *PASJ*, **44**, 55
 Hodgson, R. 1859, *MNRAS*, **20**, 15
 Hudson, H. S. 1972, *SoPh*, **24**, 414
 Jing, Z., Li, Y., Feng, L., et al. 2024, *SoPh*, **299**, 11
 Kleint, L., Heinzel, P., Judge, P., et al. 2016, *ApJ*, **816**, 88
 Kowalski, A. F., Hawley, S. L., Carlsson, M., et al. 2015, *SoPh*, **290**, 3487
 Krucker, S., Saint-Hilaire, P., Hudson, H. S., et al. 2015, *ApJ*, **802**, 19
 Le, G., Yang, X., Liu, Y., et al. 2014, *Ap&SS*, **350**, 443
 Lemen, J. R., Title, A. M., Akin, D. J., et al. 2012, *SoPh*, **275**, 17
 Li, C., Fang, C., Li, Z., et al. 2022, *SCPMA*, **65**, 289602
 Li, H., Chen, B., Feng, L., et al. 2019, *RAA*, **19**, 158
 Li, Y., Jing, Z., Song, D.-C., et al. 2024, *ApJL*, **963**, L3
 Machado, M. E., Emslie, A. G., & Brown, J. C. 1978, *SoPh*, **58**, 363
 Martínez Oliveros, J.-C., Krucker, S., Hudson, H. S., et al. 2014, *ApJL*, **780**, L28
 Neidig, D. F., & Cliver, E. W. 1983, *SoPh*, **88**, 275
 Pesnell, W. D., Thompson, B. J., & Chamberlin, P. C. 2012, *SoPh*, **275**, 3
 Poland, A. I., Milkey, R. W., & Thompson, W. T. 1988, *SoPh*, **115**, 277
 Procházka, O., Reid, A., Milligan, R. O., et al. 2018, *ApJ*, **862**, 76
 Pugh, C. E., Armstrong, D. J., Nakariakov, V. M., et al. 2016, *MNRAS*, **459**, 3659
 Romano, P., Elmhamdi, A., Falco, M., et al. 2018, *ApJL*, **852**, L10
 Saint-Hilaire, P., Schou, J., Martínez Oliveros, J.-C., et al. 2014, *ApJL*, **786**, L19
 Scherrer, P. H., Schou, J., Bush, R. I., et al. 2012, *SoPh*, **275**, 207
 Song, D.-C., Tian, J., Li, Y., et al. 2023, *ApJL*, **952**, L6
 Song, Y. L., Tian, H., Zhang, M., et al. 2018, *A&A*, **613**, A69
 Su, Y., Liu, W., Li, Y.-P., et al. 2019, *RAA*, **19**, 163
 Su, Y., Zhang, Z., Gan, W., et al. 2022, *Handbook of X-ray and Gamma-ray Astrophysics* (Berlin: Springer), 88
 Worden, S. P. 1983, in IAU Colloq. 71: *Activity in Red-Dwarf Stars*, 102, ed. P. B. Byrne & M. Rodono (Dordrecht: Reidel), 207
 Xu, Y., Cao, W., Liu, C., et al. 2004, *ApJL*, **607**, L131
 Zhang, Z., Chen, D.-Y., Wu, J., et al. 2019, *RAA*, **19**, 160